*Journal of Advanced Ceramics*
2024, **13**(10): 1643–1654
https://doi.org/10.26599/JAC.2024.9220966

Research Article

# Dual-feedback healing mechanism redefining anti-oxidation coatings in fiber-reinforced composites

Yuanshuai Wang, Xinyu Wang, Pianpian Zhang, Anqi Lun, Yuewei Li, Yi Wang, Lizhe Xing, Zhengyang Fu, Ya'nan Yang✉, Long Xia✉

*School of Materials Science and Engineering, Harbin Institute of Technology (Weihai), Weihai 264209, China*

Received: June 11, 2024; Revised: September 1, 2024; Accepted: September 1, 2024



**Abstract:** This study introduces a pioneering design concept termed the "dual-feedback healing mechanism", which investigates the relationship between oxidation products and protective coatings. Specifically, it focuses on channeling oxidation products generated at exposed cracks in the substrate to interact with the antioxidant coatings, enabling a self-repair mechanism for cracks. $BN_f$/SiBN was chosen as the ceramic matrix, while the Si–O–Al system served as the antioxidant coating. The dynamic process of obtaining Si–O–Al (SOAC) coating involving the pyrolysis of organic precursors and the dual-feedback healing mechanism were systematically investigated. These findings indicate that when the temperature surpasses 1150 °C, the exposed BN fibers at the cracks are oxidized, transforming into $B_2O_3$(g). Subsequently, $B_2O_3$(g) reacts with $SiO_2$, forming a SiBO mixture. The mixture effectively diminishes the viscosity of the coating, enabling it to flow and form a fresh protective layer that effectively blocks $O_2$ infiltration. Consequently, after oxidation at 1500 °C, the coated samples experience a mere 3% weight loss. This technology emphasizes the interconnectivity during material transformation, utilizing matrix oxidation products as a driving force for self-healing of the coating. This approach achieves intelligent-like, targeted closure of oxygen pathways, thereby pioneering a novel concept and direction for the advancement of antioxidant coatings. Consequently, this approach not only enhances our understanding of the fundamental nature of "self-healing" but also holds significant potential in the development of reparable antioxidant coatings.

**Keywords:** antioxidant coating; dual-feedback; $BN_f$/SiBN composite; Si–O–Al coating; self-healing

## 1 Introduction

The continuous advancement in contemporary aviation and precision-guided technology has sparked considerable interest in ultra-high-temperature composite materials related to applications such as missile radome and hypersonic flight [1–3]. Presently, the most advanced research has focused on $SiO_2$ fiber-reinforced ceramic matrix composes (FRCMCs). However, the crystalline phase transition of $SiO_2$ fibers at elevated temperatures may result in a sudden decline in mechanical performance [4]. To address the challenges posed by ultra-high-temperature conditions resulting from high Mach speeds, researchers have embarked on a thorough investigation into novel ceramic fibers, including $Al_2O_3$ [5–7], $Si_3N_4$ [8], SiBN [9], and even BN fibers [10]. Notably, BN fibers exhibit exceptional thermal stability, preserving structural integrity up to 1800 °C in a nitrogen atmosphere [11,12]. The ceramic matrix is also one of the main components of FRCMCs. The SiBN matrix integrates the benefits of $Si_3N_4$ and BN, exhibiting superior properties such as oxidation resistance, high-temperature strength, modulus retention, wave transmission, and ablation resistance [13]. Nevertheless, under atmospheric conditions, BN fibers and SiBN matrix can be oxidized above 1200 °C, leading to the production of $B_2O_3$ and subsequent structural degradation, thereby limiting their practical application.

In addition to the use of inherently high-temperature-resistant materials, the application of antioxidant coatings serves as an effective approach to increase the thermal stability [14–17]. The most extensively researched and applied materials are ultra-high temperature ceramic (UHTC) coatings [18–20]. These coatings primarily consist of transition metal carbides, nitrides, and borides [21,22]. The incorporation of elements such as Si, B, C, and N has significantly expanded the application range of composite materials. Zhang *et al.* [23] utilized supersonic atmospheric plasma spraying (SAPS) and reactive melt infiltration to fabricate $ZrB_2$–Si–ZrC ultra-high-temperature ceramic coatings. The coatings feature an *in-situ* oxide layer with a Si–B–O system [24], resembling the process structure of silicon carbide heating elements, allowing them to exhibit excellent oxidation resistance under 2000 K acetylene flame exposure. However, the use of transparent FRCMCs for radome applications necessitates higher requirements for oxidation-resistant coatings. Owing to the demand for effective transmission of electromagnetic waves, coatings are required for their low dielectric properties [25]. Consequently, the request significantly restricts the options available for coating systems. The Si–O–Al system, with advantages such as a low dielectric constant and the ability to transform into commonly used mullite thermal barrier coatings at high temperatures, presents itself as a viable option for the protective layer of radome materials [24]. Despite various preparation methods for FRCMCs, including hot-pressing sintering of two-dimensional non-woven fabric layers [26–28]

✉ Corresponding authors.
E-mail: Y. Yang, yangyanan310@163.com;
L. Xia, xialonghit@gmail.com



清华大学出版社 Tsinghua University Press | SciOpen

and precursor infiltration and pyrolysis (PIP) of three-dimensional woven structures [29–32], the challenge of mismatched thermal expansion coefficients between fibers and matrices persists, leading to uneven internal stress distributions [33]. Even in homogeneous reinforced composites such as $SiO_{2f}/SiO_2$ [34], there is an issue of differential axial and radial shrinkage of fibers at high temperatures. This uneven shrinkage during thermal cycling can cause cracking and even delamination of surface coating, thereby exposing the internal structure to high-temperature oxidation environments. Hence, the study of antioxidant coatings for composite materials in high-temperature oxygen environments has long been hindered by challenges in achieving effective compatibility between the coating and matrix, resulting in suboptimal design outcomes.

Multilayer composite coatings serve as one of the primary methods to mitigate the mismatch in thermal expansion coefficients [35–38]. For example, Ren *et al.* [39] applied a $ZrB_2$–SiC–$TaSi_2$–Si coating on the graphite substrate via slurry brushing and the vapor-phase silicon infiltration method. The results of the antioxidant performance test at 1500 °C indicated that the dual-phase layer structure enhanced the oxidation resistance and peeling resistance. Some studies have focused on growing unique structures within coatings to enhance their self-healing capabilities. Wang and Luo [40] employed carbon–carbon composite ceramics as the matrix and achieved *in situ* growth of SiC nanowires within a $HfB_2$–SiC–Si–SiC coating to study the high-temperature oxidation and thermal shock resistance properties. The presence of SiC nanowires was found to facilitate the healing of cracks in the coating during high-temperature exposure. These design approaches still predominantly rely on multiple coatings and have not undergone a fundamental transformation to solve the problem of cracking in antioxidant coatings, yet achieving thermal synchronization of coatings remains a challenge. The randomness of coating cracking and the mismatch between the matrix oxidation temperature as well as the self-healing temperature of the coating remain significant challenges in the field of antioxidant coatings. Furthermore, nitride FRCMCs also lack the systematic design concept for antioxidant properties and regular experimental validation.

There is an urgent need for a concept and experimental design that enables thermally synchronized and precise repair of coating cracks. Specifically, in terms of antioxidant mechanisms and antioxidative capability of materials, there might be a mechanism of reciprocal transformation between oxidation and antioxidation. The primary model of the mechanism is exemplified by silicon carbide ceramics that oxidize *in situ* to form a protective film layer, resisting further reactions with oxygen [41]. To incorporate the systematic design principles inspired by this philosophy into nitride ceramic fiber composites, this study introduces a method utilizing $BN_f$/SiBN composite materials prepared through the PIP process as the matrix, with an anti-oxidative Si–O–Al (SOAC) coating synthesized on its surface using an organic synthesis approach. Early oxidation products interact with antioxidant coatings via gas-phase transfer, forming new film layers that self-heal punctures, cracks, and voids from high-temperature oxidation. This design aims to avoid thermal expansion mismatch, fully blocks oxygen, and introduces the "dual-feedback healing" concept for enhanced protection. In an optimal state, the coating completely encapsulates the matrix. If cracks emerge during heating, high-temperature $O_2$-induced oxidation products swiftly react with the coating, inducing it to flow and seal the cracks, thereby preventing additional $O_2$ penetration. This work verifies the oxidative damage to $BN_f$/SiBN composite materials, elucidates the formation mechanism of the dual feedback coating, and assesses the reliability of the "dual feedback coating" in antioxidative coating systems. Furthermore, the "dual feedback coating" exhibits high design flexibility, allowing the creation of different coating systems tailored to various material systems. This leads to the development of a semi-continuous high-temperature self-forming coating design system, offering a novel approach for high-temperature antioxidative protection in composite materials.

## 2 Experimental

### 2.1 Materials

The raw materials for preparing $BN_f$/SiBN composites include BN fibers and polysilborazane (PBSZ). BN fibers were purchased from Shandong Industrial Ceramic Research and Design Institute, China. PBSZ (viscosity < 200 MPa·s) was purchased from the Institute of Chemistry, Chinese Academy of Sciences, China. The raw materials for preparing the SOAC composite include hydrogen-containing silicone oil, pure silane coupling agent, and isopropanol aluminum. The hydrogen-containing silicone oil (XC202, hydrogen content ≥ 1.6%) was purchased from Xingchi Chemical Co., Ltd., China. Silane coupling agent (KH550, 99%) and isopropanol aluminum (analytical grade) were supplied by Macklin Reagent, China.

### 2.2 Composite ceramic matrix

$BN_f$/SiBN FRCMCs were fabricated through multiple impregnation, curing, and pyrolysis cycles of the fiber preform. The specific procedure is detailed in the Electronic Supplementary Material (ESM).

### 2.3 Coating preparation

The SOAC was prepared through a multi-step spraying process, as illustrated in Fig. 2. Initially, 5 wt% isopropanol aluminum solution was prepared using ethanol as the solvent. Subsequently, KH550 was added to the solution at a mass ratio of 1 wt%, resulting in mixed solution A. The hydrogen-containing silicone oil was referred to as solution B. The spraying sequence followed pattern A–B–A. After application, the coatings were cured at low temperatures and pyrolyzed at medium-to-low temperatures. The detailed procedure is provided in the ESM. The cured SOAC@$BN_f$/SiBN samples were heated at 150, 300, 450, 550, and 700 °C for 0.5 h to observe the organic-to-inorganic transformation process of the coatings.

### 2.4 Oxidation texting

Oxidation tests were conducted in an oxygen atmosphere. The $BN_f$/SiBN composite materials without coatings were subjected to oxidation tests at 1200, 1400, and 1500 °C for 5 min, and their microstructures and mechanical properties were observed. Samples with sprayed coatings were exposed to 1500 °C for 5 min to observe their microstructure and investigate the improvement effects of the dual-feedback healing mechanism on the oxidation resistance of the material.

### 2.5 Characterization

The phase composition of the sample was analyzed via an X-ray diffractometer (XRD; X'pert, PROMPD, PANalytical, the Netherlands) with Cu Kα radiation (λ = 1.54 Å). The microstructures and morphologies of $BN_f$/SiBN composites and SOAC@$BN_f$/SiBN composites under different oxidation conditions were observed by a scanning electron microscope

(SEM; SUPRA 55, Zeiss, Germany). The phase structure after high-temperature treatment was observed by a high-resolution transmission electron microscope (HRTEM; JEOL-2100, JEOL, Japan). The element composition and molecular state were detected by X-ray photoelectron spectroscopy (XPS) using an Escalab 250Xi electron spectrometer (Thermo Kalpha, USA) with Al Kα radiation. The bonding of the $BN_f$/SiBN composites was analyzed via a Fourier transform infrared spectrometer (FTIR, Nicolet iS5, Thermo Scientific, USA). The weight loss variation of the material with increasing temperature was measured via a simultaneous thermal analyzer (thermogravimetry–differential scanning calorimetry (TG–DSC); STA 449F3 thermal analyzer, Netzsch, Germany), and the test gas atmosphere used was air, with a specific temperature range of 50–1499 °C. The heating rate was set at 20 °C/min. The flexural strength of the composites was measured via a three-point bending test with a sample size of 40 mm × 4 mm × 3 mm and a span of 30 mm at a loading rate of 0.5 mm/min by a Universal Materials Tester (UMT, Instron 5967, USA).

## 3 Results and discussion

### 3.1 Oxidation mechanism of $BN_f$/SiBN composite

Figure 1 illustrates the microstructural changes of $BN_f$/SiBN composite materials sintered and oxidized for 5 min at 1200, 1400, and 1500 °C. As shown in Fig. 1(a), the cross-section of the unoxidized sample displays a tight bond between the fibers and the matrix, but with a few cracks and interface fractures related to uneven stress. The limited pores observed are associated with pulled-out fibers. Figure 1(b) presents the microstructural image after oxidation at 1200 °C. Pores near the outer fibers result from oxidation, and as oxygen permeates, internal fibers gradually oxidize into a semi-open pore structure. Figure 1(c) shows the SEM image after oxidation at 1400 °C. Numerous oxidation pores have developed due to the reaction between BN and $O_2$, resulting in the generation of $N_2$(g), $B_2O_3$(l), and $B_2O_3$(g). The disappearance of the BN fibers is attributed to oxidation. In cases of excess oxygen, the oxidation reactions between the fibers and the matrix are represented by Eqs. (1) and (2). The depth of oxygen penetration can be indicated by the depth of the pores, and the depth of oxygen penetration is approximately 100 μm at 1400 °C. Figure 1(d) shows the SEM image at 1500 °C, revealing the occurrence of matrix collapse in the outer cross-section layer of the composite material. Oxidative degradation can be categorized into three stages. In the initial phase of oxidation, $O_2$ accumulates on the outer surface of the fiber and gradually permeates into its interior, constituting the first stage. Subsequently, oxygen accumulates in the pores left after fiber oxidation, and it can expand radially from the region to the surrounding areas, representing the second stage. As the external energy continues to intensify, the expanding region gradually enlarges until the phenomenon of matrix collapse occurs, marking the third stage.

$$4BN + 3O_2 = 2B_2O_3 + 2N_2 \quad (1)$$

$$4SiBN + 7O_2 = 4SiO_2 + 2B_2O_3 + 2N_2 \quad (2)$$

Figures 1(e)–1(h) depict the microscopic transformation process of the composite material during the oxidation process after 5 min at 1200 °C. Figure 1(f) shows an enlarged image of Fig. 1(e), and Fig. 1(h) an enlarged image of Fig. 1(g). Figure 1(e) illustrates the transformation zone of oxidation infiltration, with pores left by oxidized fibers and unoxidized fibers on the right. As shown in Fig. 1(f), oxidized fibers are marked in yellow, while the oxidized matrix is highlighted in purple. The oxidation reaction of BN results in the appearance of pores inside fibers with a diameter of approximately 1 μm. Additionally, the SiBN matrix also exhibits a network-like structure due to oxidation. Further oxidation of BN fibers is depicted in Figs. 1(g) and 1(h). As the oxidation reaction progresses, the fibers transform into a small

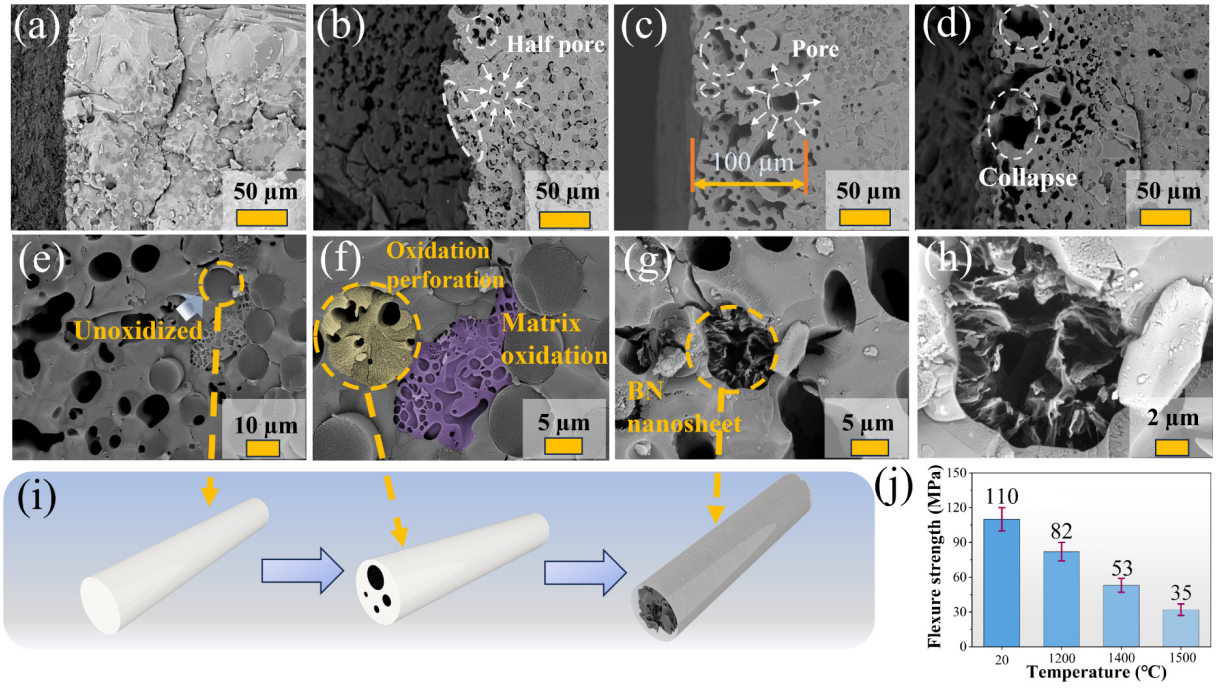


**Fig. 1** Structural changes of $BN_f$/SiBN composite material under oxidation at different temperatures: (a) unoxidized, (b) 1200 °C, (c) 1400 °C, (d) 1500 °C, (e) interface transition at 1200 °C, (f) magnified view of oxidation interface, (g) fiber oxidation structure, and (h) magnified view of fiber oxidation structure. (i) Fiber oxidation transition process, and (j) flexural strength at different temperatures.

number of BN nanosheets adhering to the inner wall of the matrix. With continued reaction, the fibers completely disappear, leaving behind only fiber channels. The transformation process of fibers during high-temperature oxidation is visually represented (Fig. 1(i)). The oxidation reaction between $O_2$ and the composite material at high temperatures causes significant damage to the structure. This damage adversely affects the mechanical properties of the material, as illustrated in Fig. 1(j).

### 3.2 Dynamic transformation of SOAC

Under high-temperature, oxygen-rich conditions, structurally stable BN is susceptible to oxidation, leading to structural failure [42]. The oxidation product $B_2O_3$ can further evolve into gaseous $B_2O_3$ at high temperatures. Considering gas-phase mass transfer, a dynamic protective mechanism is designed to interact with gaseous $B_2O_3$. This mechanism facilitates the directional flow of the antioxidant coating to the oxidation site, directing repairs in a targeted manner. At elevated temperatures, $B_2O_3$ reacts with $SiO_2$ to form low-viscosity SiBO. Moreover, mullite possesses both high-temperature stability and the ability of its $SiO_2$ component to react with the oxidized product $B_2O_3$, thereby establishing a dynamic dual-feedback healing mechanism. This mechanism enhances the antioxidant performance of $BN_f$/SiBN materials. Hence, a straightforward spray method was employed to apply organic Si and Al sources onto the material surface. By controlling the temperature, these sources transform from organic to inorganic SOAC. The preparation process is illustrated in Fig. 2. To achieve suitable coating curing conditions, an investigation into the dynamic process of the coating transition from organic to inorganic was conducted. Subsequently, a detailed analysis was performed on the dynamic protective mechanism and antioxidative capabilities of the dual-feedback healing mechanism after oxidation.

To investigate the transformation process of organosilicon and isopropyl aluminum during the preparation of the Si–O–Al coating, XRD, and FT-IR analyses were conducted on SOAC@$BN_f$/SiBN composites sintered at different temperatures. Figure 3(a) shows the XRD patterns at 150, 300, 450, 550, and 700 °C. As depicted, the diffraction peaks of the composite materials at various temperatures are wide and stable, indicating that the Si–O and Al–O bonds are unable to form a crystalline structure at medium to low temperatures. The diffraction pattern exhibits a low-intensity peak at approximately $2\theta$ = 27.5°, as depicted in Fig. 3(a1), with a broad peak region with $2\theta$ spanning from 26° to 28°, which may be attributed to the presence of BN microcrystals within the BN fibers (PDF#45-0896, $2\theta$ = 26.8°, (002)). The broad diffraction peak makes it challenging to distinguish the composition phases of the material effectively. Nevertheless, this confirms that no crystalline structure is formed during the transition from organic to inorganic coating, indicating a significant advantage for the coating to effectively adhere to the substrate surface [43].

Figure 3(b) presents the FT-IR spectra of SOAC@$BN_f$/SiBN composite materials at different sintering temperatures. As shown in Fig. 3(b), the absorption peak at approximately 750 $cm^{-1}$ is attributed to the symmetric stretching vibration of the Si–O group [10], the peak at 920 $cm^{-1}$ corresponds to the stretching vibration of the Si–N bond [44], and the peak near 1380 $cm^{-1}$ represents the stretching vibration of the B–N bond [45]. The Si–N and B–N bonds are intrinsic chemical bonds present in the $BN_f$/SiBN material, which indicates the presence of a SiBN matrix and BN fibers within the composite material. With the introduction of organic silicon, Si–O bonds are inevitably present during the transition of the organic silicon coating. The peak at 1080 $cm^{-1}$ corresponds to the asymmetric stretching vibration of the Al–O bond, and the peak near 3000 $cm^{-1}$ represents the bending vibration of the C–H bond in the alcohol salt. When the temperature increases to 600 °C, the C–H bond disappears, indicating the complete oxidation of the organic components at this temperature. Similarly, the disappearance of the C–O bond at 1200 $cm^{-1}$ with increasing temperature further confirms the process of organic transformation.

Figure 3(c) shows the schematic transformation of the coating. In the ambient temperature state, the organic mixture of hydrogen-containing silicone oil and aluminum isopropanol is uniformly coated on the substrate surface. As the temperature increases to 300–600 °C, the coating begins to transform from organic to inorganic, resulting in the formation of particle-like agglomerations of –Al–O– and –Si–O– bonds. With further temperature increase, these bonds transform into an inorganic coating that uniformly covers the substrate. Additional confirmation of this transformation can be obtained through SEM analysis.

Figure 4 illustrates the dynamic transformation process of the SOAC. Figures 4(a1)–4(e1) present cross-section images of SOAC@$BN_f$/SiBN composites at 150, 300, 450, 550, and 700 °C. Figures 4(a2)–4(e2) show enlarged views of Figs. 4(a1)–4(e1), while Figs. 4(a3)–4(e3) display the region of the surface coating. The series of SEM images dynamically illustrate the transformation of the coating from organic to inorganic. As shown in Figs. 4(a1) and 4(a2), the Si–O–Al organic coating exhibits outstanding film-forming properties at 150 °C and is tightly integrated with the $BN_f$/SiBN substrate interface. As depicted in Fig. 4(a3), the SOAC exhibits no cracks. Figures 4(b1) and 4(b2) depict cross-sectional images of the SOAC coating after 300 °C, revealing that the coating remains undisturbed and predominantly comprises organic material at this temperature. Figure 4(b3) exhibits the gradual emergence of cracks on the surface coating, suggesting the initiation of cracking stemming from thermal mismatch mechanisms. The coating has initiated a

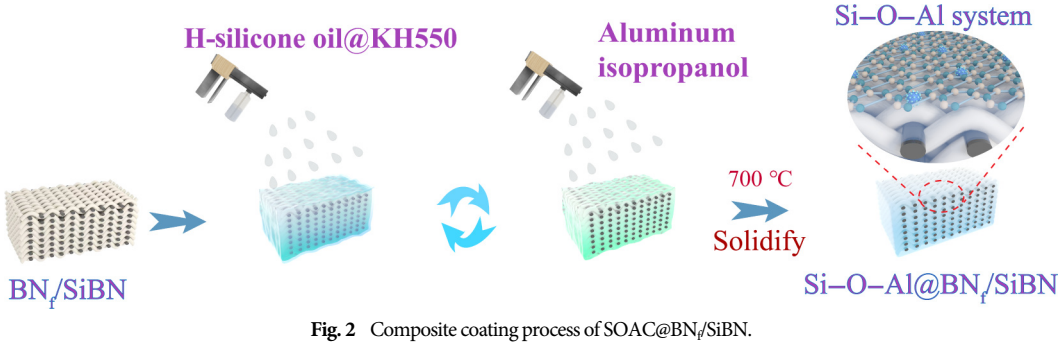


**Fig. 2** Composite coating process of SOAC@$BN_f$/SiBN.

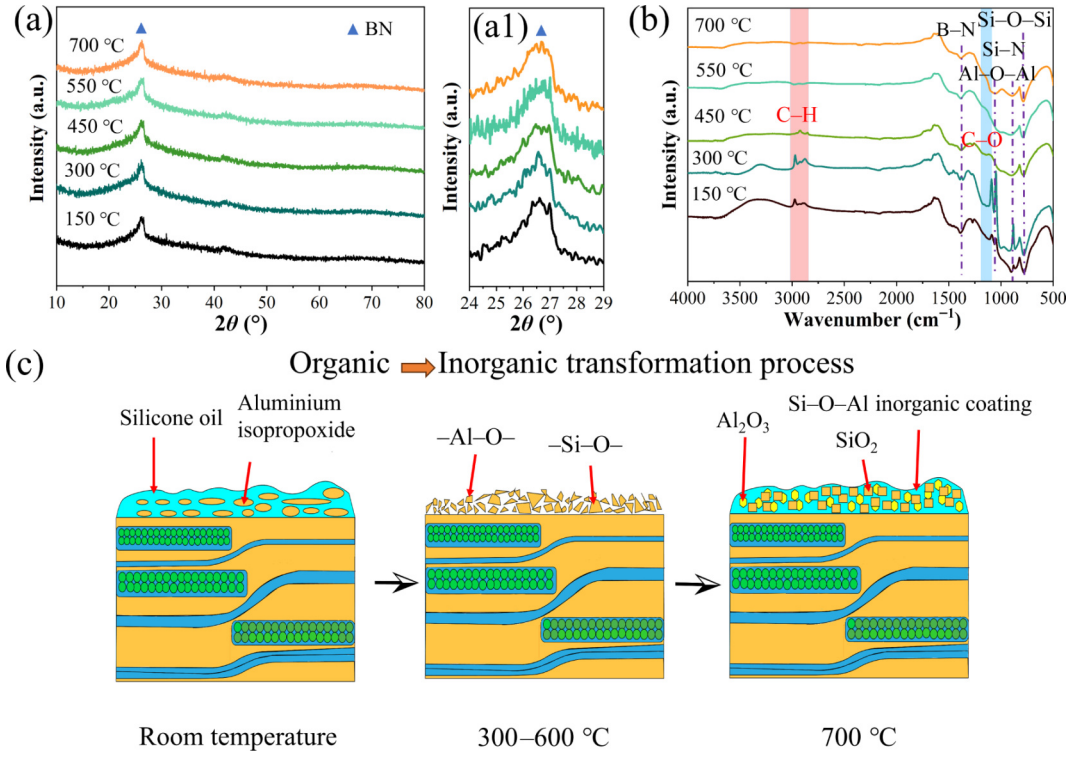


**Fig. 3** Phase transition of SOAC under dynamic temperature changes: (a) XRD pattern, (a1) an enlarged view in range of 25°–28° from (a), (b) FT-IR spectra, and (c) schematic representation of coating transition.

transition from organic to inorganic at this stage. The microstructure observed at 450 °C, as shown in Fig. 4(c1), clearly demonstrates the most pronounced transition from organic to inorganic, with the organic coating transforming particles that cover the surface of the substrate. Figure 4(c2) shows that the agglomerated particles consist of smaller particles, which are presumed to be inorganic remnants of Al–O and Si–O particles. Figure 4(d1) depicts images of the cross-sectional coating at 550 °C. At this temperature, the outer layer particles undergo thermal oxidation, transitioning into an inorganic film. However, owing to the limited external energy input, inorganic particles are unable to form a complete film. When the temperature decreases to room temperature, contraction occurs in the substrate because of thermal mismatch. In addition, the surface of the film layer warps, which is attributed primarily to the failure of the binding force between the fine particles and the matrix to overcome the surface tension of the film layer. Figure 4(d3) also shows that there is a tendency for the film layer to detach from the surface. The final microstructure of the film layer sintered at 700 °C is shown in Fig. 4(e1). During this stage, the surface inorganic particles have completely transformed into an inorganic film layer, which exhibits good bonding with the interface. Inevitably, microcracks appear (Fig. 4(e3)). However, the $BN_f$ and SiBN matrices exhibit good thermal stability, posing no risk of oxidation in air at 700 °C.

The EDS spectrum of the coating transformation process for SOAC@$BN_f$/SiBN is presented in Fig. 5. Figure 5(a) shows the cross-section at 150 °C, indicating that Si element is distributed in areas other than the fibers, while Al and O elements are exclusively present exclusively on the surface of the coating. Figure 5(b), on the other hand, depicts the cross section at 450 °C, revealing the presence of Al, O, and Si within the region and confirming that the agglomerated particles are composed of Al–O and Si–O components. Figure 5(c) presents the cross-section image at 550 °C, where the warped surface is visibly composed of Si, Al, and O elements, confirming that it is a Si–O–Al coating.

### 3.3 Dual-feedback healing anti-oxidation mechanism

The cross-sectional microstructure of the SOAC@$BN_f$/SiBN composite material after oxidation is shown in Fig. 6(a). Owing to the protective effect of the surface coating, the composite material has a small number of micropores and defects, yet the internal fiber structure remains relatively intact at ultra-high temperatures. Similarly, the cross-section of the $BN_f$/SiBN composite material without coating under the same oxidation conditions is depicted in Fig. 6(b). Owing to oxidation, BN fibers leave numerous pores in situ. At elevated temperatures, the presence of the coating can be categorized into three forms. The first form is referred to as the "perfect protection state", where the coating remains continuous and free of cracks during oxidation. Combined with the excellent bonding performance between the inorganic coating and the substrate observed in Fig. 4(e1), it is evident that the majority of the material is in the first form. As depicted in Fig. 6(c), when the coating is oxidized at high temperatures, molten mullite is generated *in situ*, covering the surface of the substrate. Figure 6(d) shows an enlarged view of Fig. 6(c), which shows that the interface tightly bonded with the fiber effectively acts as a barrier to prevent oxygen, thus preserving the integrity of the fiber at ultra-high temperatures. The second form is referred to as the "dual-feedback healing mechanism in progress", which often occurs at locations where cracks appear due to thermal mismatch. At ultra-high temperatures, $O_2$ first enters the interior of the coating, fibers, and substrate through cracks, initiating oxidation reactions. As a result, the BN fibers sustain damage due to oxidation. Simultaneously, the $SiO_2$ in the surface mullite layer is stimulated by the escape of $B_2O_3$(g), leading to a decrease in viscosity and promoting its flow toward oxidation defects. As illustrated in Figs. 6(e) and 6(f), the coating flows downward from the top, comprehensively encompassing the front end of the BN fiber. Nevertheless, certain areas where the coating is insufficient remain. The third form is the "completion state of the dual-

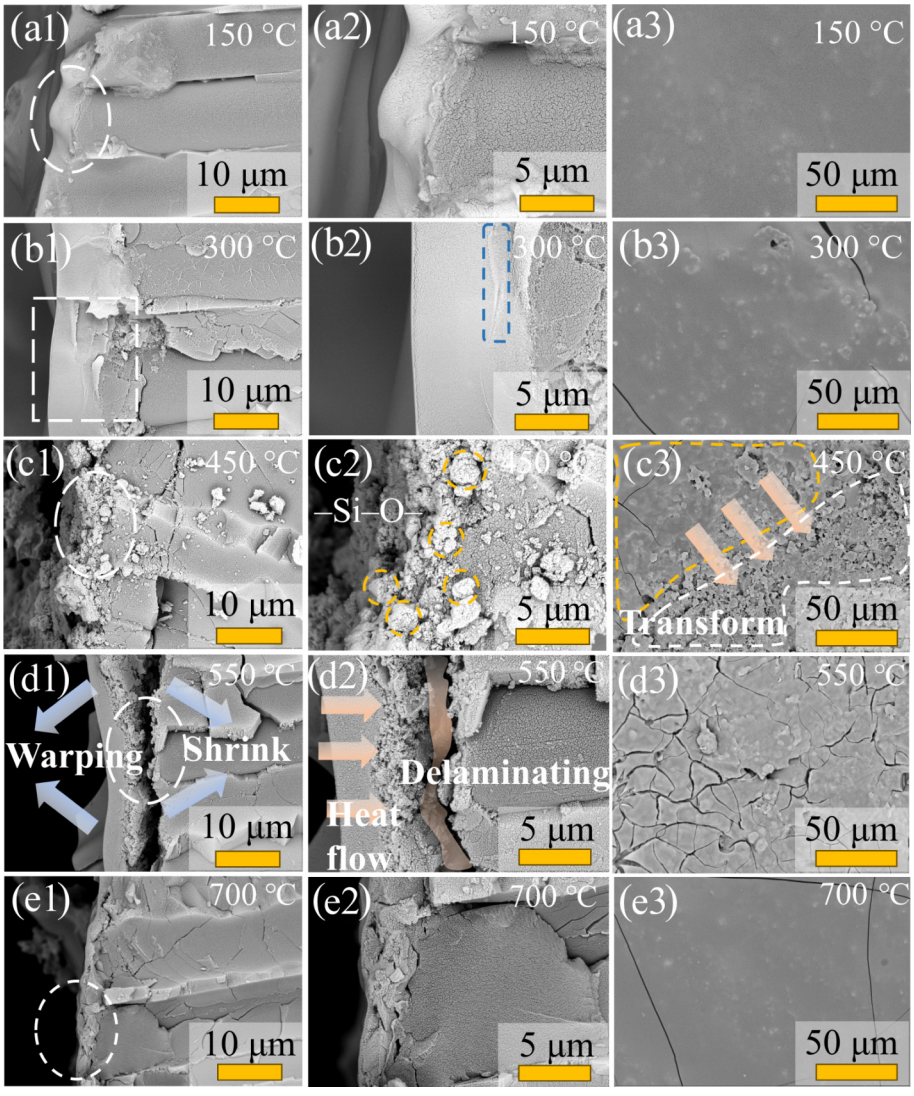


**Fig. 4** SEM images of dynamic transformation process of SOAC sintered at different temperatures: (a) 150 °C, (b) 300 °C, (c) 450 °C, (d) 550 °C, and (e) 700 °C. (X1) represents the cross-section, and (X2) is a magnified view of (X1), with the magnified area indicated by white box. (X3) shows surface of (X1) (X = a, b, c, d, and e).

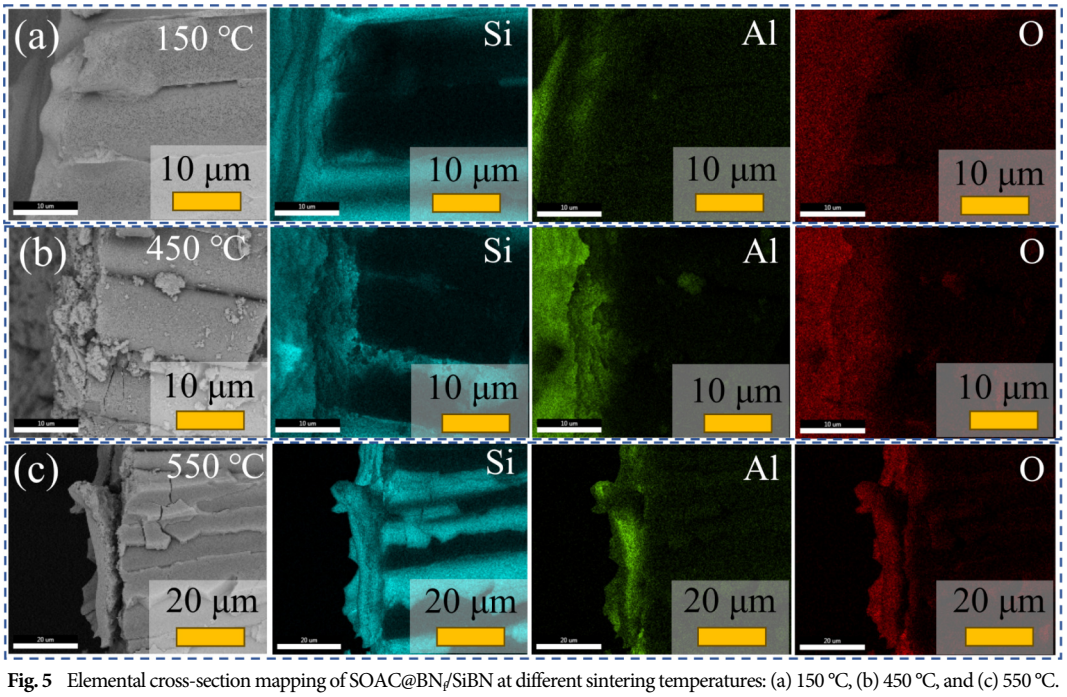


**Fig. 5** Elemental cross-section mapping of SOAC@$BN_f$/SiBN at different sintering temperatures: (a) 150 °C, (b) 450 °C, and (c) 550 °C.

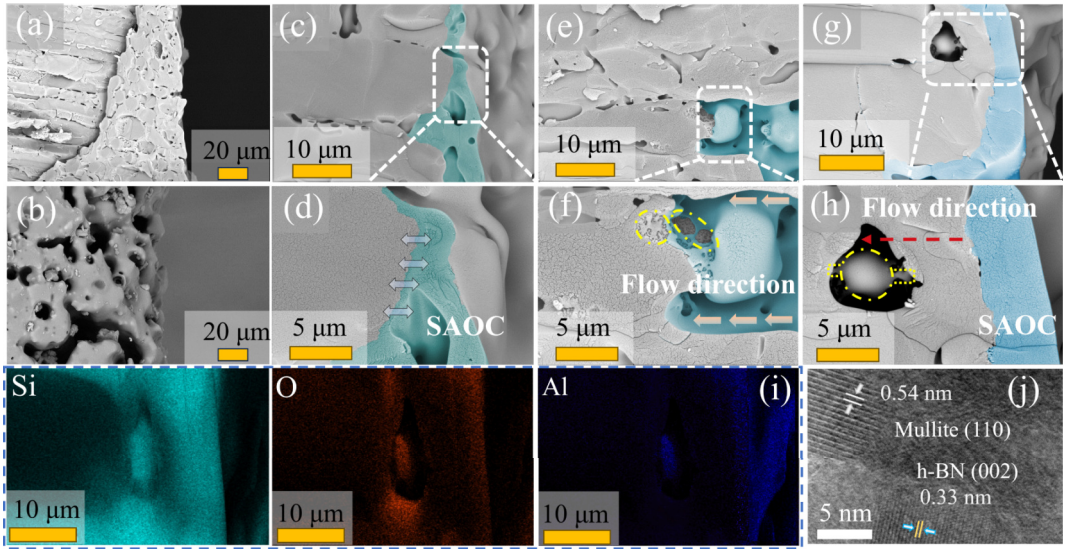


**Fig. 6** Microstructure of SOAC@$BN_f$/SiBN after high-temperature oxidation at 1500 °C for 5 min: (a) cross-section of SOAC@$BN_f$/SiBN, (b) cross-section of $BN_f$/SiBN, (c) perfectly protected state of coating and substrate, (d) local magnification of (c), (e) state of dual-feedback healing, (f) local magnification of (e), (g) completion of dual-feedback healing, (h) local magnification of (g), (i) elemental spectra of Si, O, and Al, and (j) HRTEM image of interface between SOAC and BN fibers.

feedback healing mechanism", as shown in Figs. 6(g) and 6(h). Through the pores in the matrix section, it can be observed that the internal coating has completely enveloped the front end of the fiber and extends downward along the fiber direction. EDS was employed to investigate the distribution of Si, Al, and O elements, and it is evident from Fig. 6(i) that Si element is uniformly distributed in both the matrix and coating. Oxygen element is distributed within the coating as well as at the interface between the oxidized fiber matrix. Owing to the susceptibility of the SiBN matrix to oxidation at high temperatures, oxygen tends to penetrate along fiber cracks toward the matrix. The element aluminum is mainly distributed on the surface of the coating and at the interface between the coating and the matrix. The elemental distribution further corroborates the distribution status of the coating within the matrix. The interface bonding and lattice coherence between the BN fibers and SOAC were observed via HRTEM to provide a more comprehensive investigation. As shown in Fig. 6(j), the BN lattice fringe is measured to be 0.33 nm, corresponding to the (002) crystal face, and the mullite lattice fringe measures 0.54 nm and corresponds to the (110) crystal face [46]. Figure S2 in the ESM presents the lattice fringe patterns of the two phases. In addition, Fig. 6(j) also indicates a strong affinity between h-BN and the mullite phase coating, effectively impeding oxygen penetration.

The phase composition of SOAC@$BN_f$/SiBN after oxidation at 1500 °C for 5 min followed by air cooling is presented in Fig. 7. Figures 7(a) and 7(b) show the XRD and FT-IR patterns, respectively, after the high-temperature oxidation reactions. As shown in Fig. 6(a), strong diffraction peaks at $2\theta$ = 21.9° for the (101) crystal plane and $2\theta$ = 26.3° for the (200) crystal plane correspond to cubic $SiO_2$ (PDF#39-1425). During air cooling, $SiO_2$ within SOAC@$BN_f$/SiBN transforms into the cubic phase, while other phases remain in an amorphous state. A weak and broad peak is observed in the $2\theta$ range of 26°–28°, encompassing the (120) plane ($2\theta$ = 25.9°) and (210) plane ($2\theta$ = 26.2°) of the mullite orthorhombic system (PDF#39–1425), as well as the (002) plane of BN ($2\theta$ = 26.8°). The broad peak suggests the formation of fine microcrystalline nuclei within the material. However, owing to the excessively rapid cooling rate in air, the amorphous state is unable to stabilize into crystals. Therefore, in addition to cubic $SiO_2$, the BN fibers retain their microcrystalline amorphous state, and the SOAC maintains its amorphous state at high temperatures. Figure 7(b) shows the FT-IR spectrum of SOAC@$BN_f$/SiBN after a high-temperature oxidation reaction. Multiple absorption peaks are observed in the spectrum. The absorption peak near 750 $cm^{-1}$ is attributed to the symmetric stretching vibration of Si–O–Si bond, which is attributed primarily to $SiO_2$ within the SOAC and the oxidized trace amounts of $SiO_2$ at the cracks. The peak at 920 $cm^{-1}$ corresponds to the stretching vibration of Si–N bond, indicating the stable existence of the SiBN matrix despite the oxidation process. The peak at approximately 1380 $cm^{-1}$ is assigned to the stretching vibration of B–N bond, indicating that BN fibers still exist after oxidation. The position of the Si–O–B stretching vibration is located near 1450 $cm^{-1}$ [47]. Additionally, the peak at 1080 $cm^{-1}$ corresponds to the asymmetric stretching vibration of the Al–O bond, which is attributed primarily to the oxidized mullite coating.

To investigate the chemical states of the SOAC@$BN_f$/SiBN composite material after oxidation, the interface between the coating and the substrate was ground into powder, and XPS was used to analyze the chemical states at the interface. The full XPS spectrum is shown in Fig. S3 in the ESM. As shown in Figs. 7(c)–7(h), different elements were further analyzed by curve fitting with the Gauss–Lorentz equation. C 1s, as shown in Fig. 7(c), can be divided into three peaks corresponding to the O–C=O bond, C–O–C bond, and C–C bond. The three carbon peaks are attributed mainly to external carbon contamination sources. The Si 2p peak can be divided into three peaks, with the highest and most intense peak located at 102.7 eV attributed to the Si–O bond in the mullite phase. Another two weaker peaks are located at 101.9 eV, attributed to the Si–N bond in SiBN, and at 103.5 eV, attributed to the Si–O bond in $SiO_2$ [48]. The Al 2p orbital exhibits a single peak at 74.4 eV, attributed to the Al-O bond in the mullite phase [49]. This indicates that after high-temperature oxidation, the Al–O and Si–O bonds in the coating have reacted to form the mullite phase. The O 1 s peak can be divided into two components: a weaker O–Al bond at approximately 531.1 eV, associated with mullite, and a stronger O–B bond at approximately 532.5 eV, related to $B_2O_3$. The strong O–B peak is attributed to the oxidation of $B_2O_3$ in BN and SiBN, while the

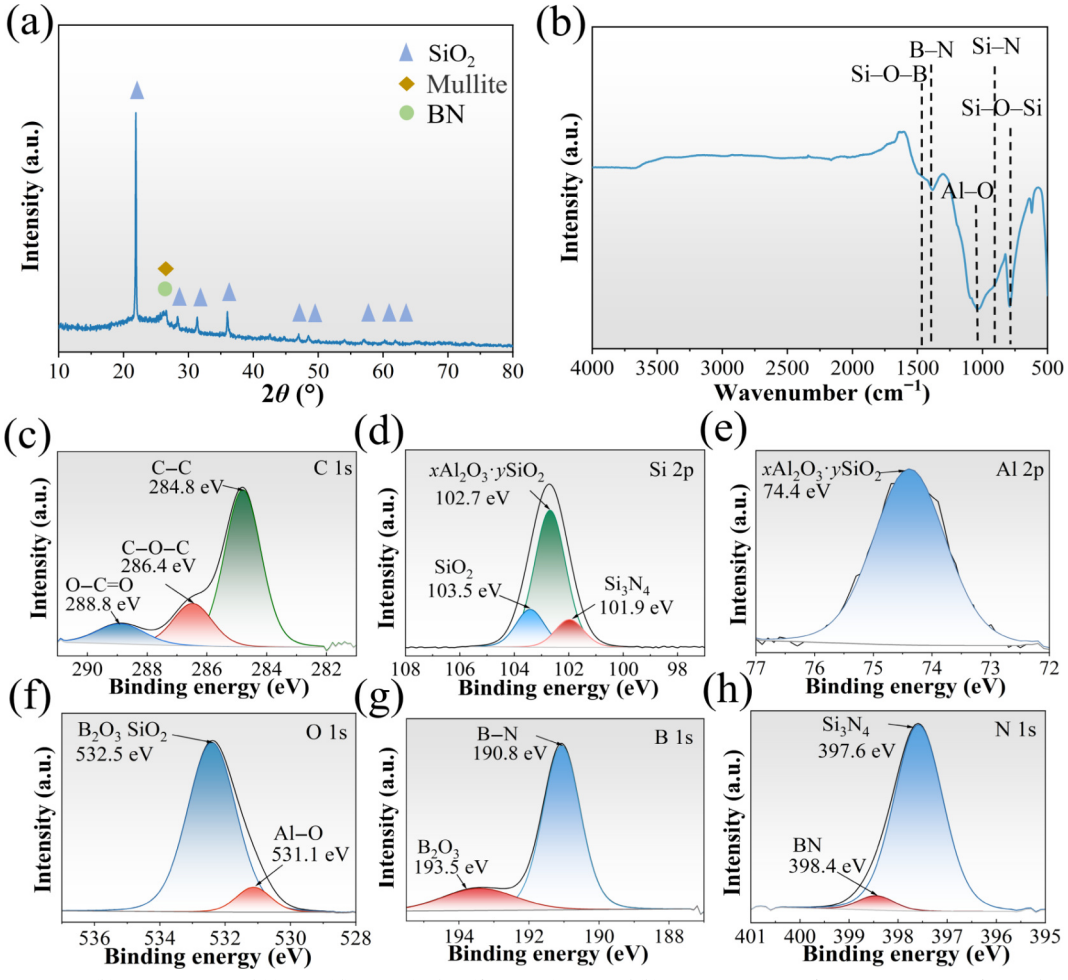


**Fig. 7** (a) XRD pattern, (b) FTIR pattern and (c) C 1s, (d) Si 2s, (e) Al 2s, (f) O 1s, (g) B 1s, and (h) N 1s XPS spectra of SOAC@BN$_f$/SiBN after oxidation at 1500 °C.

O–Si peak is associated with surface mullite and $SiO_2$ [50]. The B 1s orbital exhibits two peaks: a strong peak at approximately 190.8 eV, which is attributed mainly to the strong B-N bond from the BN fibers and the SiBN matrix, and a weaker peak at approximately 193.5 eV, which is attributed to the B-O bond provided by $B_2O_3$ [51]. In the N 1s spectrum, the strong peak at 397.6 eV originates from the Si–N bond provided by $Si_3N_4$, while the weaker peak at 398.4 eV arises from the N–B bond [52]. XPS analysis indicates that the Al-O bonds in the membrane have almost entirely transformed into the mullite phase. Although a small portion of the BN fibers or SiBN matrix has undergone oxidation to generate $B_2O_3$, the majority of the matrix and fibers remain intact and are protected by the Si–O–Al layer. The oxidized phase further affirms the outstanding protective role of the dual-feedback healing mechanism against substrate oxidation.

The thermal behavior of BN$_f$/SiBN and coated SOAC@BN$_f$/SiBN composites was investigated through TG–DTA testing, and the results are presented in Figs. 8(a) and 8(b). Figure 8(a) depicts the TG–DTG curve of BN$_f$/SiBN. The weight loss of the material within the temperature range of 50–1500 °C can be divided into two distinct stages. In the first stage, a gradual weight loss with a relatively flat DTG spanning from 150 to 750 °C is observed, which is attributed primarily to the evaporation of crystal water absorbed by unprotected BN$_f$/SiBN and the oxidative volatilization of residual organic compounds. The second stage occurs from 1150 to 1500 °C, during which the rate of weight loss significantly accelerates, and the weight loss is approximately 11.5%. The corresponding DTG curve steeply decreases, reaching a maximum peak at 1300 °C. The weight loss is attributed to the oxidation of the BN$_f$/SiBN matrix, resulting in the volatilization of oxidation products such as $B_2O_3$(g) and $N_2$(g) [53]. Consequently, the rate of weight loss can also reflect the rate of oxidation. The oxidation reaction begins at 1150 °C and reaches its maximum rate at 1300 °C. The oxidation rate subsequently decreases with increasing temperature. The decrease in the oxidation rate is attributed to the amorphous $B_2O_3$(l) produced during the oxidation of BN and SiBN, which acts as an oxygen barrier. As the quantity of oxidation products reaches a sufficient level, they hinder the continued penetration of oxygen. Consequently, the overall weight loss rate ultimately reaches 20%. Figure 8(b) presents the TG–DTG curve of SOAC@BN$_f$/SiBN. The weight loss of the material within the temperature range of 50–1500 °C can be divided into three distinct stages. The first stage occurs from 100 to 500 °C and represents the transition of the coating from organic to inorganic materials. The second stage spans from 770 to 850 °C. During this stage, a slight increase in mass is observed. This is attributed to the residual traces of incompletely oxidized Si–O and Al–O within the coating reacting with oxygen in the air. The third stage occurs between 1150 and 1500 °C, during which the BN$_f$/SiBN composite also undergoes oxidation. However, even when the temperature reaches 1500 °C, no oxidation peak is observed. This is attributed to the crucial role played by the dual-feedback healing mechanism. The oxidation product, $B_2O_3$(g), reduces the viscosity of the mullite coating. Once $B_2O_3$ is generated, the low-viscosity mullite coating can block the oxygen channel, leading to a dynamic cycle of oxidation

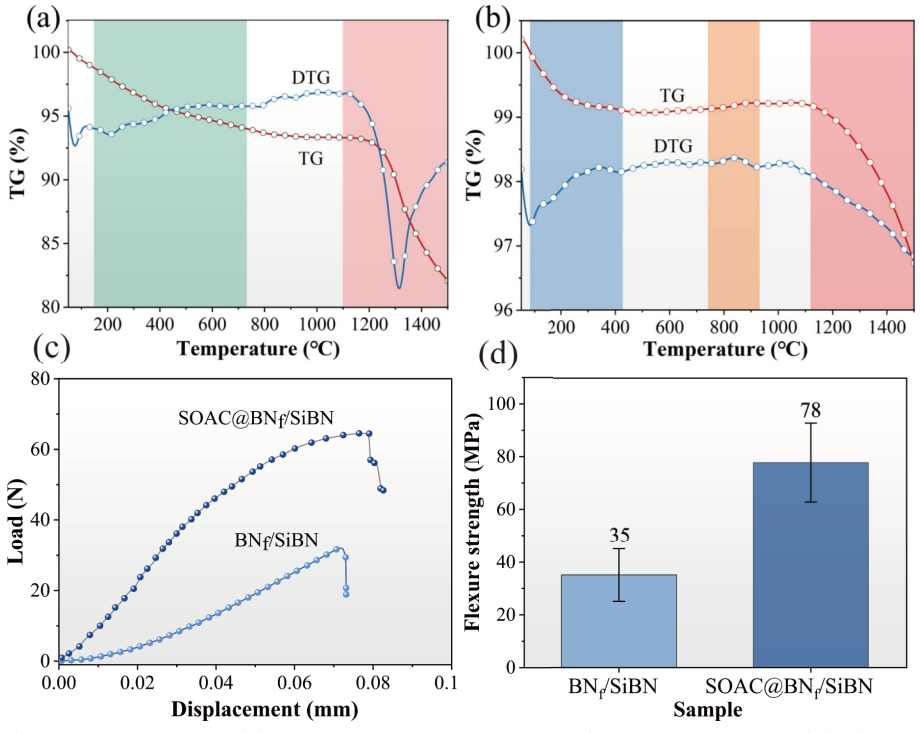


**Fig. 8** TG–DTG curves of (a) $BN_f$/SiBN composite and (b) SOAC@$BN_f$/SiBN composite, ranging from 50 to 1500 °C. (c) Load–displacement curves of $BN_f$/SiBN and SOAC@$BN_f$/SiBN composite oxidized at 1500 °C. (d) Flexural strengths of $BN_f$/SiBN and SOAC@$BN_f$/SiBN composites oxidized at 1500 °C.

and sealing of the oxygen channel in the $BN_f$/SiBN. This dynamic cycle enhances the antioxidant properties of the material, resulting in a weight loss rate of only 3% in the temperature range of 50–1500 °C. The classical load–displacement curves and flexural strengths of $BN_f$/SiBN composite and SOAC@$BN_f$/SiBN composite after oxidation at 1500 °C are depicted in Figs. 8(c) and 8(d), respectively. Owing to the internal structural damage to the $BN_f$/SiBN composite after oxidation, the material exhibits brittle fracture characteristics with a flexural strength of 35 MPa. In contrast, the SOAC@$BN_f$/SiBN composite demonstrates pseudo-ductile fracture characteristics, with its flexural strength still maintaining at 78 MPa after oxidation, which is attributed to the protective effect of the dual-feedback self-healing mechanism of SOAC on $BN_f$/SiBN.

The temperature variation of the $B_2O_3$–$SiO_2$ binary oxide system is illustrated in Fig. 9. Herein, s quartz-low represents the low-temperature quartz phase; s2 quartz-high denotes the high-temperature quartz phase; s2 tridymite signifies the tridymite phase; and s6 cristobalite indicates the cristobalite phase. The transition points among these phases are illustrated in Fig. 9. The eutectic temperature at which the two phases exhibit the lowest melting point is determined to be 438 °C. Below this temperature, any mixture of $B_2O_3$–$SiO_2$ at any molar ratio consists predominantly of $B_2O_3$(s) and $SiO_2$(s quartz-low). As the temperature increases, a mixture of the liquid slag phase (slag-liq) and $SiO_2$ phase gradually appears. When the temperature exceeds 1465 °C, a mole fraction of 5% $B_2O_3$ is sufficient to completely form the liquid slag phase (slag-liq) in the SiBO system. The dual-feedback healing mechanism is also constructed based on the melting behavior of the $B_2O_3$–$SiO_2$ system. The minimum oxidation temperature of BN fibers is approximately 1150 °C, indicating that the oxidation reaction to produce $B_2O_3$ occurs only when the ambient temperature exceeds this threshold. Owing to the influence of gas partial pressure, gaseous $B_2O_3$ forms when the temperature exceeds 1200 °C. As gaseous $B_2O_3$ permeates toward

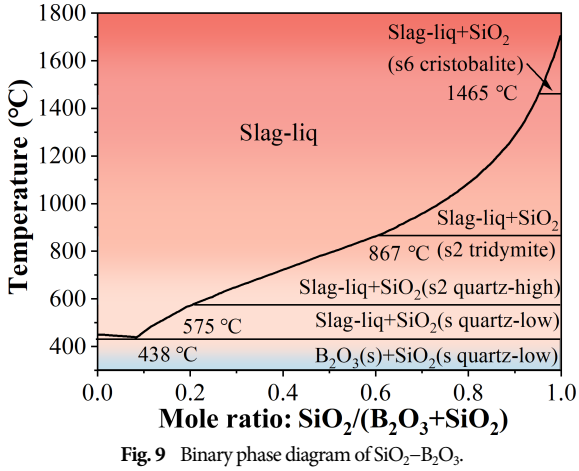


**Fig. 9** Binary phase diagram of $SiO_2$–$B_2O_3$.

the outer surface, it reacts with the surface $SiO_2$ to form borosilicate compounds. Since these reactions occur at temperatures above 1200 °C, even a small amount of $B_2O_3$ can facilitate the transformation of the SiBO system into a liquid slag phase (slag-liq). Moreover, as the $B_2O_3$ content gradually increases, the proportion of the liquid slag phase (slag-liq) also increases. Therefore, the rate of the dual-feedback healing mechanism depends more on the oxidation rate of the internal $BN_f$/SiBN composite material. The faster the material is oxidized, the faster the crack repair rate of the membrane layer is, creating a mutually constrained behavior that can act as a perfect protective mechanism.

The dual-feedback healing mechanism, established to bypass the impact of thermal mismatch, is depicted in Fig. 10. The dynamic oxidation process is illustrated as (a) → (b) → (d) in the dual-feedback healing mechanism, primarily occurring at locations where cracks appear in the antioxidative membrane. Figure 10(a) depicts the unoxidized region, where cracks are

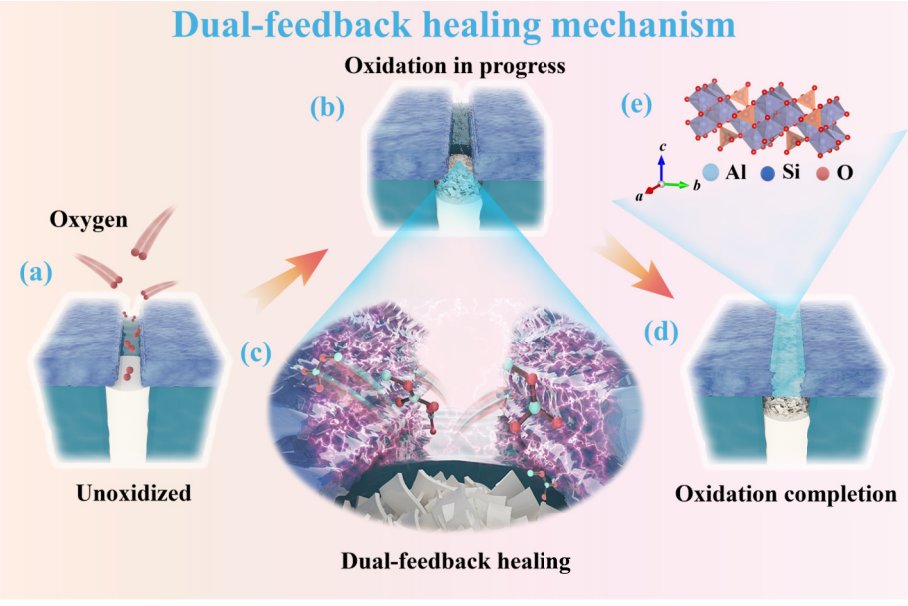


**Fig. 10** Schematic diagram of dual-feedback healing mechanism in SOAC@$BN_f$/SiBN: (a) unoxidized SOAC@$BN_f$/SiBN cracks under an oxygen atmosphere, (b) initial oxidation structure of SOAC@$BN_f$/SiBN fibers under an oxygen atmosphere, (c) micro-dynamic process of dual-feedback mechanism, (d) self-repairing morphology of dual-feedback cracks, and (e) crystal structure of mullite coating.

formed due to the mismatch in the thermal expansion coefficients between the oxidation film and the substrate. These cracks expose a small amount of the internal matrix and fibers to the air, providing a pathway for oxygen. In an ultra-high-temperature environment, oxygen enters the interior of the substrate through the oxygen channel, reacting with the BN fibers and SiBN substrate to produce $N_2$(g), $SiO_2$(l), $B_2O_3$(l), and $B_2O_3$(g). At this point, the liquid-phase $SiO_2$ and liquid-phase $B_2O_3$ flow into the gaps of the substrate, while $N_2$ and gaseous-phase $B_2O_3$ rise and are expelled from the substrate, as illustrated in Fig. 10(b). During the escape process, $B_2O_3$(l) contacts $SiO_2$ in the SOAC, resulting in a reduction in its viscosity. This process is depicted in Fig. 10(c). The molecular structure of the mullite layer is depicted in Fig. 10(e). The mullite layer with a reduced viscosity then flows toward the fiber defects, gradually repairing and bridging the cracks caused by the thermal mismatch mechanism. Once the cracks are completely sealed, the oxygen transmission channels are blocked, effectively preventing the ingress of oxygen. Subsequently, the formation of oxidative products such as $B_2O_3$(g) is hindered, allowing the mullite layer to return to a stable state, as shown in Fig. 10(d). The advantage of the dual-feedback healing mechanism lies in its ability to achieve a self-repairing effect dynamically through the oxidation of the substrate. The oxidation products of the substrate or fibers at the crack locations provide positive feedback to the coating, thereby impeding oxygen ingress and facilitating coating healing. The oxidation-repair mechanism perfectly circumvents the issue of continuous oxidation of the internal material caused by the mismatch in the coefficient of thermal expansion.

## 4 Conclusions

This research systematically investigated the oxidation mechanism of BN ceramic fibers in $BN_f$/SiBN composite materials under thermal field coupling. In addition to addressing the unavoidable issue of antioxidant coating cracking on the surface of fiber composites at elevated temperatures due to mismatched thermal expansion coefficients, the design concept of the dual-feedback healing mechanism is proposed. The oxidation products occurring at coating cracks can be directed to feed back into the coating, inducing a mechanism where the coating undergoes spontaneous physical or chemical reactions to self-heal and repair the cracks. This study explores the dynamic impact process of the BN fiber oxidation product $B_2O_3$(g) on SOAC, confirming that this design concept can establish a reaction mechanism of coating cracking, initial oxidation, feedback to the coating, and directed bridging. The application of the dual-feedback healing mechanism design concept allows for the fabrication of SOAC@$BN_f$/SiBN composite materials capable of maintaining an intact internal structure at 1500 °C. Furthermore, this design concept holds universal value, as it provides a novel approach for addressing the issue of antioxidant coating cracking and filling the application gap of $BN_f$-reinforced ceramic matrix composites in thermal–oxygen coupling environments.

## Acknowledgements

We acknowledge the financial support from the National Natural Science Foundation of China (No. 51972078), the Heilongjiang Touyan Team Program, the Fundamental Research Funds for the Central Universities (No. HIT.OCEF.2021003), and the Key Laboratory of Advanced Structural-Functional Integration Materials & Green Manufacturing Technology.

## Declaration of competing interest

The authors have no competing interests to declare that are relevant to the content of this article.

## Electronic Supplementary Material

Supplementary material is available in the online version of this article at https://doi.org/10.26599/JAC.2024.9220966.

## References

[1] Lyu Y, Han ZH, Zhao GD, *et al.* Efficient fabrication of light $C_f$/SiHfBOC composites with excellent thermal shock resistance and ultra-high-temperature ablation up to 1800 °C. *J Adv Ceram* 2023, **12**: 2062–2074.

[2] Yang XJ, Li B, Li D, *et al.* High-temperature properties and interface

evolution of silicon nitride fiber reinforced silica matrix wave-transparent composite materials. *J Eur Ceram Soc* 2019, **39**: 240–248.
[3] Zhang W, Su L, Lu D, *et al.* Resilient $Si_3N_4$@$SiO_2$ nanowire aerogels for high-temperature electromagnetic wave transparency and thermal insulation. *J Adv Ceram* 2023, **12**: 2112–2122.
[4] Xiang Y, Wang Q, Peng ZH, *et al.* High-temperature properties of 2.5D $SiO_{2f}$/$SiO_2$ composites by sol–gel. *Ceram Int* 2016, **42**: 12802–12806.
[5] Wang S, Luo F, Guo J, *et al.* Effect of preparation conditions on mechanical, dielectric and wave-transparent properties of $Al_2O_{3f}$/mullite composites. *J Mater Sci Mater Electron* 2022, **33**: 20317–20327.
[6] Wen J, Xiang Y, Zhang W, *et al.* Ablation behavior of coated $Al_2O_{3f}$/$Al_2O_3$ composites under oxyacetylene torch flame. *Adv Appl Ceram* 2022, **121**: 23–30.
[7] Xiang Y, Zhang W, Chen K, *et al.* High-temperature mechanical property and thermal shock resistance of $Al_2O_{3f}$/$Al_2O_3$ composites. *Int J Appl Ceram Tec* 2022, **19**: 3267–3278.
[8] Zhou J, Cheng LF, Ye F, *et al.* The control of interfacial bonding state and optimization of mechanical properties of $Si_3N_{4f}$/BN/$Si_3N_4$ composites via different synthesis technologies. *J Eur Ceram Soc* 2021, **41**: 1739–1746.
[9] Long X, Wu ZY, Shao CW, *et al.* High-temperature oxidation behavior of SiBN fibers in air. *J Adv Ceram* 2021, **10**: 768–777.
[10] Meng FX, Li W, Du YA, *et al.* Insight into the evolution process from novel polyborazine precursor PPMAB to inorganic BN fiber. *Ceram Int* 2022, **48**: 33373–33380.
[11] Li YG, Liu XF, Dong LH, *et al.* Preparation and high-temperature service performance of hierarchically pore-structured BN fiber aerogels. *Ceram Int* 2022, **48**: 36287–36296.
[12] Tay RY, Li HL, Wang H, *et al.* Advanced nano boron nitride architectures: Synthesis, properties and emerging applications. *Nano Today* 2023, **53**: 102011.
[13] Liu Y, Peng S, Cui YJ, *et al.* Fabrication and properties of precursor-derived SiBN ternary ceramic fibers. *Mater Des* 2017, **128**: 150–156.
[14] Liu DB, Shi BL, Geng LY, *et al.* High-entropy rare-earth zirconate ceramics with low thermal conductivity for advanced thermal-barrier coatings. *J Adv Ceram* 2022, **11**: 961–973.
[15] Wei ZY, Meng GH, Chen L, *et al.* Progress in ceramic materials and structure design toward advanced thermal barrier coatings. *J Adv Ceram* 2022, **11**: 985–1068.
[16] Yuan K, Tu TZ, Shen C, *et al.* Self-ball milling strategy to construct high-entropy oxide coated $LiNi_{0.8}Co_{0.1}Mn_{0.1}O_2$ with enhanced electrochemical performance. *J Adv Ceram* 2022, **11**: 882–892.
[17] Chen L, Meng GH, Li CJ, *et al.* Critical scale grain size for optimal lifetime of TBCs. *J Mater Sci Technol* 2022, **115**: 241–250.
[18] Ni DW, Cheng Y, Zhang JP, *et al.* Advances in ultra-high temperature ceramics, composites, and coatings. *J Adv Ceram* 2022, **11**: 1–56.
[19] Zhang L, Padture NP. Inhomogeneous oxidation of $ZrB_2$–SiC ultra-high-temperature ceramic particulate composites and its mitigation. *Acta Mater* 2017, **129**: 138–148.
[20] Chen L, Luo JC, Yang WQ, *et al.* Durable dual-state duplex Si–$HfO_2$ with excellent oxidation and cracking resistance. *J Adv Ceram* 2024, **13**: 388–401.
[21] Fahrenholtz WG, Hilmas GE. Oxidation of ultra-high temperature transition metal diboride ceramics. *Int Mater Rev* 2012, **57**: 61–72.
[22] Zheng LY, Li HP, Zhou J, *et al.* Layer-structured Cr/$Cr_xN$ coating via electroplating-based nitridation achieving high deuterium resistance as the hydrogen permeation barrier. *J Adv Ceram* 2022, **11**: 1944–1955.
[23] Zhang YL, Hu H, Zhang PF, *et al.* SiC/$ZrB_2$–SiC–ZrC multilayer coating for carbon/carbon composites against ablation. *Surf Coat Tech* 2016, **300**: 1–9.
[24] Qiu JY, Montecillo R, Chen PY, *et al.* Development of the $Al_2O_3$–$B_2O_3$–$SiO_2$ glass for thermal barrier coating. *J Non-Cryst Solids* 2024, **626**: 122785.
[25] Meng N, Liu CD, Ye F, *et al.* Effects of heating rate on mechanical and dielectric properties of the $Si_3N_4$f/BN/$Si_3N_4$ composites by PIP. *J Mater Res Technol* 2023, **22**: 3463–3474.
[26] Ai JP, Zhou GH, Zhang HL, *et al.* Mechanical properties and microstructure of two-dimensional carbon fiber reinforced zirconia composites prepared by hot-pressing. *Ceram Int* 2014, **40**: 835–840.
[27] Liu YJ, Wang J, Jing R, *et al.* Improving mechanical properties of continuous carbon fiber-reinforced $ZrB_2$–$ZrSi_2$ composite by addition of activated carbon. *Mater Lett* 2024, **357**: 135645.
[28] Liu YX, Cheng YH, Ma DH, *et al.* Continuous carbon fiber reinforced $ZrB_2$–SiC composites fabricated by direct ink writing combined with low-temperature hot-pressing. *J Eur Ceram Soc* 2022, **42**: 3699–3707.
[29] Jia LT, Wang MQ, Guo XF, *et al.* Effect of chemical vapor infiltration on the flexural properties of C/C–SiC composites prepared by the precursor infiltration pyrolysis method. *New Carbon Mater* 2023, **38**: 1127–1134.
[30] Lee SH, Weinmann M, Aldinger F. Processing and properties of C/Si–B–C–N fiber-reinforced ceramic matrix composites prepared by precursor impregnation and pyrolysis. *Acta Mater* 2008, **56**: 1529–1538.
[31] Zhang L, Wang WQ, Gao X, *et al.* Additive manufacturing of continuous carbon fiber reinforced high entropy ceramic matrix composites via paper laminating, direct slurry writing, and precursor infiltration and pyrolysis. *Ceram Int* 2023, **49**: 7833–7841.
[32] Zhou J, Ye F, Cheng LF, *et al.* Microstructure and mechanical properties of $Si_3N_{4f}$/BN/$Si_3N_4$ composites by joint processes of PIP and CVI. *Mater Sci Eng A* 2022, **844**: 142988.
[33] Reynaud P, Rouby D, Fantozzi G. Effects of temperature and of oxidation on the interfacial shear stress between fibres and matrix in ceramic-matrix composites. *Acta Mater* 1998, **46**: 2461–2469.
[34] Zhang YT, Fan XY, Yang Z, *et al.* Fabrication and high-temperature strength of 2.5D $SiO_{2f}$/$SiO_2$ composites prepared by a combined vacuum impregnation and sol–gel method. *Ceram Int* 2023, **49**: 36199–36205.
[35] Duan ZX, Deng LH, Lü KY, *et al.* Thermal cycle and water oxygen performance of multi-layered $Y_3Al_5O_{12}$/$Yb_2SiO_5$/$Yb_2Si_2O_7$ thermal/environmental barrier coatings. *Ceram Int* 2024, **50**: 16309–16317.
[36] Feng T, Li HJ, Wang SL, *et al.* Boron modified multi-layer $MoSi_2$–$CrSi_2$–SiC–Si oxidation protective coating for carbon/carbon composites. *Ceram Int* 2014, **40**: 15167–15173.
[37] Hu D, Fu QG, Liu B, *et al.* Multi-layered structural designs of $MoSi_2$/mullite anti-oxidation coating for SiC-coated C/C composites. *Surf Coat Tech* 2021, **409**: 126901.
[38] Li YY, Liu YC, Guo C, *et al.* Ablation resistance of ZrC-based composite coating with multi-layer structure for carbon/carbon composites above 2200 °C. *Corros Sci* 2022, **207**: 110600.
[39] Ren Y, Qian YH, Xu JJ, *et al.* Oxidation and cracking/spallation resistance of $ZrB_2$–SiC–$TaSi_2$–Si coating on siliconized graphite at 1500 °C in air. *Ceram Int* 2020, **46**: 6254–6261.
[40] Wang TY, Luo RY. Oxidation protection and mechanism of the $HfB_2$–SiC–Si/SiC coatings modified by *in situ* strengthening of SiC whiskers for C/C composites. *Ceram Int* 2018, **44**: 12370–12380.
[41] Li L, Yu Y, Yang JS, *et al.* A $ZrB_2$–SiC(Al) coating with improved oxidation resistance for C/C composites: Design, experimental verification and oxidation mechanism. *J Eur Ceram Soc* 2024, **44**: 3487–3500.
[42] Wang JT, Yang ZM, Yang R, *et al.* High-temperature transient-induced thermomechanical damage of fiber-reinforced ceramic–matrix composites in supersonic wind tunnel. *Compos Part A—Appl S* 2024, **184**: 108243.
[43] Wan ZF, Liu Y, Sang SB, *et al.* Fracture behavior of lightweight mullite–SiC refractories with porous aggregates coated with glass ceramic. *Ceram Int* 2022, **48**: 32273–32282.

[44] Long X, Shao CW, Wang YD. The formation of chemical/structural gradients in strong covalent bonded SiBN fibers under active nitrogen atmosphere. *J Eur Ceram Soc* 2021, **41**: 3333–3340.
[45] Hou YB, Yang XJ, Li B, *et al.* Preparation and interface modification of $Si_3N_{4f}/SiO_2$ composites. *J Mater Sci Technol* 2019, **35**: 2767–2771.
[46] Zhan LJ, Wu CZ, Zhang FQ, *et al.* Coordinated regulation for α-$Al_2O_3$ and mullite structures in the alumina–mullite fiber based on the different adding form of Fe element. *J Eur Ceram Soc* 2024, **44**: 4185–4195.
[47] Li D, Yu QP, Li XC, *et al.* Study on the fiber/matrix interface modification of $Si_3N_{4f}/SiO_2$ composites with polymer derived double-layer coatings. *J Eur Ceram Soc* 2023, **43**: 7381–7389.
[48] Li ZH, Sun J, Zhang X, *et al. In-situ* mullite whisker reinforced SiC porous ceramics with whiskers and bonding layers synchronously growing: Using $CaF_2$ as a temperature-controlled whisker formation switch. *J Eur Ceram Soc* 2024, **44**: 3470–3478.
[49] Abenojar J, Colera I, Martínez MA, *et al.* Study by XPS of an atmospheric plasma-torch treated glass: Influence on adhesion. *J Adhes Sci Technol* 2010, **24**: 1841–1854.
[50] Lei YP, Wang YD, Song YC, *et al.* Nearly stoichiometric BN fiber with low dielectric constant derived from poly(alkylamino)borazine. *Mater Lett* 2011, **65**: 157–159.
[51] Chen LY, Huang MX, Luo T, *et al.* A low-temperature route to nanocrystalline boron nitride whiskers and flakes. *Mater Lett* 2004, **58**: 3634–3636.
[52] Zhang XY, Li XM, Xing XD. Effect of $B_2O_3$ content on viscosity and structure of $SiO_2$–MgO–FeO-based slag. *T Nonferr Metal Soc* 2022, **32**: 2403–2413.
[53] Zhao LF, Cao WD, Li YJ, *et al.* Improved thermal shock and oxidation resistance of β-SiAlON incorporated with h-BN. *J Alloys Compd* 2023, **947**: 169686.